RSC Advances

PAPER

View Article Online
View Journal | View Issue

Cite this: *RSC Adv.*, 2026, **16**, 9769

A study on the structural arrangements and compositional changes in laser-stabilized metastable AlO_x/C nanocomposites

Elijah M. Davis[ac] and Dibyendu Mukherjee *[bc]

Amorphous metal oxides hold promising and yet, untapped potential as new classes of functional engineering materials due to their long-range disordered structures. While such disruptive features are alluring, fundamental understanding of structure–composition properties during their disorder-to-order transitions hold the key to their rational design as novel functional materials. Recently, we employed laser ablation synthesis in solution (LASiS) to kinetically entrap amorphous and metastable Al-oxide (a-AlO_x) nanostructures with non-stoichiometric compositions ($x \sim 2.5–3.0$) that indicated remarkable stability from carbon interfaces. In this work we provide detailed insights into thermally induced phase change characteristics and structural evolution of these highly disordered a-AlO_x/C nanocomposites (NCs) using Atomic Pair Distribution Function (PDF) analyses from X-ray scattering experiments. Our results indicate that the ultra-small AlO_x nanostructures evolve from highly disordered to low-order polycrystalline structures while undergoing Al–O bond re-arrangements indicating coordination shifts during each step of high-temperature (>500–800 °C) phase transition. We also demonstrate our ability to tailor the composition (x = O/Al ratio) and percentage crystallinity in these NCs by varying the laser flux within accessible ranges by comparing two discrete nanosecond pulse durations (5 ns and 9 ns) during LASiS; this paves the path for ability to regulate their energy release and trapped oxidative gas contents in their design as solid-state phase change materials (SS-PCMs) in energetic applications. These studies provide critical insights into the stability and structural bond re-arrangements in metastable a-AlO_x/C NCs undergoing disorder-to-order transitions during high temperature isothermal phase change processes. Such studies pave a novel path for the future design and development of advanced SS-PCM based energetic additives as intrinsic initiators/oxidizers in next-generation solid propellant formulations.

Received 15th October 2025
Accepted 4th February 2026

DOI: 10.1039/d5ra07897k

rsc.li/rsc-advances

1. Introduction

Amorphous and disordered inorganic materials constituting random atomic arrangements have gained significant attention in the materials research community due to their unique characteristics, such as intrinsic isotropy, defect distribution, structural flexibility, metastable states and high porosity. Yet, their applications have not been fully revealed due to contentious debates regarding the correlation between this lack of order and specific functionality in these classes of materials. Specifically, amorphous metals oxide (a-MO_x) nanostructures trapped in non-equilibrium phase spaces and in a metastable state have increasingly indicated superior electrocatalytic, charge transfer and ion intercalation properties in electrochemical energy storage/conversion systems. However, reliable and experimentally viable non-equilibrium synthesis routes to achieve such kinetic entrapment of metastable molecules remain elusive, with most attempts employing ultra-fast quenching, physical/chemical deposition, high-pressure compression or shock, and mechanical attrition techniques.[1,2] The non-equilibrium reaction pathways in all these techniques are initiated by increasing the internal entropy of the target metal through rapid energy dumping and quenching before they transition to their final stable oxide form. Yet, these processes often demand elaborate and cumbersome experimental set-ups that are not conducive to scale-ups. Recent years have seen laser ablation synthesis in solution (LASiS) emerge as one of the few known facile methods that can effectively induce the kinetic entrapment of nanoscale metastable oxides while being amenable to large scale production due to the simplicity of the technique and the rapid advancements in laser technologies.

It has been long-postulated that the highly non-equilibrium nature of LASiS processes architected by the high-T/high-P dense plasmas arising from the rapid and focused dumping of ultra-short high-energy laser pulses followed by their

[a]*Department Nuclear Engineering, University of Tennessee, Knoxville, TN, USA*
[b]*Department of Chemical, Environmental & Materials Engineering, University of Miami, Coral Gables, FL, USA. E-mail: dxm1936@miami.edu*
[c]*Nano-BioMaterials Lab for Energy, Energetics & Environment (nbml-E3), University of Miami, Coral Gables, FL, USA*

immediate quenching by surrounding room temperature liquids promote this kinetic trapping of metastable states. Furthermore, the technique offers the unique capabilities of simultaneously tailoring the structure–composition properties of the as-synthesized NCs which could also shed light on its ability to tune the non-equilibrium reaction conditions. LASiS has a few non-independent synthesis parameters, including laser fluence, wavelengths, repetition rates, and pulse widths, to tune the laser plasma properties whereas solvent choice, duration of ablation, solvent temperatures, and solvent chemical precursors to the solution-phase reactions. Each of these parameters can cooperatively affect the laser ablation and laser-induced pyrolytic processes that can in turn alter and tailor the final phase, compositions, structures, size/morphology and disorder/defects in the as-synthesized nanoparticles, thereby offering a diverse library of complex and functional nanomaterials.[3–10] Our group has developed, patented and demonstrated the rigors of a technique termed as LASiS-GRR that interfaces LASiS as the rate-controlling step to produce primary NPs from high-energy laser plasmas with simultaneous galvanic replacement reactions (GRR) as the rate-limiting step in solution-phase, to produce complex and composite nanostructured materials. We have successfully established the technique's versatility in tailoring sizes, shapes, structures and interfacial properties of core–shell metal, metal oxide/hydroxide NPs in amorphous, crystalline and metastable phases[11–15] as well as, control compositions/degrees of alloying for diverse intermetallic/alloyed NCs,[16–18] nanoporous frameworks, and hybrid NCs.[19–21]

In recent years, a growing interest in new classes of metallized energetic nanomaterials have inspired our group to use LASiS techniques for synthesizing Al-based composite and metastable nanoparticles stabilized *via* interfacial carbon coatings that prevent parasitic surface oxidations, while allowing them to release chemical energy during their transformation into stable oxides. Specifically, we have employed LASiS using Al targets under acetone or toluene to synthesize graphitic-C coated Al NPs that indicated that high laser fluence (>3–10 J cm^{-2}) and solvent specific vapor pressures play significant roles in tailoring the ensuing particle sizes and structures.[13] In a series of curious follow-up experiments, it was observed that LASiS under low laser fluence conditions (<1.0–1.2 J cm^{-2}) phase-stabilized unusually hyper-oxidized and metastable a-AlO_x/C NCs ($2.5 < x \leq 3.5$) comprising highly disordered a-AlO_x nanostructures (<10 nm) that were remarkably stabilized by ordered interfacial C-monolayer atoms. The a-AlO_x structures underwent volume shrinkages during their solid–solid phase transition into stable θ/γ-Al_2O_3 polymorph crystallites at temperatures >750 °C, while releasing excess trapped gases (O_2, CO_2, CO). A relatively large activation barrier was observed for this phase transformation *via* disproportionation reaction that was comparable to those for the oxidation of micron-sized Al particles, thereby explaining their unusual stability. Such observations beg the obvious need for fundamental investigations into the structural bond re-arrangements that ensue during the disorder-to-order transitions of these metastable nanostructures into their equilibrium phase states.

It is well-known that crystalline to crystalline solid–solid phase change materials (SS-PCMs) do not release enough stored energy to be useful for energetic applications.[22] In contrast, disordered amorphous structures transitioning to their first nucleated crystallites would presumably release more energy due to the accompanying entropic compensation from the disorder-to-order transition.[22] Hence, designing the aforesaid a-AlO_x/C NCs as energetic SS-PCMs would likely require the ability to tailor the extent of crystallinity, disorder, and composition of the a-AlO_x structures since a higher degree of disorderliness would justifiably promote higher amounts of trapped bond strain energies whereas, the O : Al ratios in these materials would determine the amount of trapped gases in them that, in turn, can tune their energetic and oxidative gas yields. Theoretical studies have found only a handful of Al_xO_y ($y/x > 1.5$) structures to be stable with their negative formation energies (E_f) being a function of cluster sizes and the O : Al ratios.[23] For energetic applications, it would obviously be desirable to stabilize a metastable phase with as small a negative value of E_f as possible to allow for a large energy release upon their transition to stable Al_2O_3 phases. Hence, tailoring the non-stoichiometric atomic ratios in such Al_xO_y clusters by tuning the LASiS energy required to trap the desired state is crucial in designing their energy dissipation processes. Past computational studies indicated that the laser fluence (J cm^{-2}) and the resulting plasma temperature regimes during LASiS dictate the formation of Al-oxide species, with an increased AlO_x ($x > 1.5$) formation at lower laser fluences.[24] Other studies have also indicated that metal ablation under high oxygen content solvents such as methanol largely resulted in fully oxidized particles as compared to the generation of more pure metallic/carbide-like structures under toluene.[25] Additionally, laser pulse widths can significantly alter the laser plasma driven reaction kinetics to drive the pyrolysis and re-crystallization processes in various organic solvents to form various carbonaceous structures.[26] These studies posit that the choice of solvents and laser flux (fluence per unit pulse width) can be of paramount importance in architecting the structure–composition properties of disordered metastable a-MO_x nanoparticles and their carbon interfaces; consequentially, these locked-in properties determine the ensuing structural bond re-arrangement mechanisms en route to their stable equilibrium oxide phases.

2. Experimental methods

Metastable amorphous aluminum oxide/carbon nanocomposites (a-AlO_x/C NCs) were synthesized using laser ablation synthesis in organic solvents (LASiS). Two separate Q-switched Nd:YAG pulsed lasers were employed: a Brilliant Easy laser operating at 1064 nm with a 5 ns pulse width and a 10 Hz repetition rate, and a Quantel CFR 450 operating at 1064 nm with a 9 ns pulse width and a 30 Hz repetition rate, with maximum output energies up to 360 and 200 mJ per pulse respectively. The laser beams were focused onto a high-purity aluminum target (99.95% purity, 0.65 × 0.65 cm purchased from Kurt J. Lesker) submerged in acetone (>99.9% pure, Sigma-Aldrich, < 0.1% H_2O by volume) contained in a sealed quartz

vessel. Prior to ablation, nitrogen gas was bubbled in the solvent to reduce dissolved oxygen content. All ablations were carried out at ambient temperature in a constant solvent volume of 35 mL for 10 min. The laser flux was varied between 0.11 and 0.31 J cm^{-2} ns^{-1} which was adjusted using the laser pulse energy. For the final experiments, a flat-top beam shaper was introduced into the optical path to redistribute the Gaussian beam profile into a more uniform intensity distribution across the ablation spot. This was done to minimize the high-flux central region responsible for ejecting parasitic crystalline Al fragments and to reduce the low-flux periphery where little or no ablation occurs, thereby improving the overall homogeneity and reproducibility of the synthesized nanocomposites.

Following ablation, the suspended NPs were centrifuged at 4700 rpm for 10 min and the gathered NPs were dried overnight under vacuum prior to analyses. Under the benchtop LASiS configuration used here, typical productivity is ~60 mg h^{-1}. Although a higher-throughput production approach is possible which has been described in a previous publication, the present study focuses on mechanistic understanding and parameter sensitivity rather than throughput optimization.[12] The as-synthesized AlO_x/C nanocomposites prepared under the same LASiS conditions were found to have an average diameter of ~5–15 nm based on TEM-based distribution study, which has been reported in detail in our previous publication.[12] Atomic pair distribution function (PDF) analyses were carried out using data collected on a Malvern PANalytical Empyrean diffractometer with a Ag radiation source and a PIXcel detector. After collecting the X-ray total scattering (including both Bragg and diffuse contributions), the data was converted to the reduced pair distribution function, $G(r)$, *via* Fourier transformation. The PDF reports the probability of finding atom pairs separated by distance r and therefore provides local/medium-range structural information that is especially useful for amorphous and highly disordered nanomaterials, complementing phase identification by XRD. The spectra for each PDF analysis were gathered for total acquisition time of ~14 h with repeated scans to improve signal quality as detailed in Metz *et al.*[27] The data collected was refined with the Malvern PANalytical HighScore package using a custom batch-processing program. The instrumental uncertainty in extracted peak positions is ~0.01 Å; across all conditions the first-neighbor Al–Al peak position remains constant within this uncertainty, whereas the Al–O peak shifts by more than 0.01 Å, indicating that the observed Al–O changes exceed instrumental noise. To probe different stages of structural evolution several transition steps were chosen and fresh samples were heated to distinct isothermal conditions selected. The first transition step is obtained by heat treating the as-synthesized a-AlO_x/C samples at ~550 °C for 3 h before measuring the atomic pair distribution re-arrangements. In the initial as synthesized sample, it was difficult to differentiate between possible carbon compounds and the Al–O and Al–Al bond distances we were investigating. The atomic re-arrangements initiated at the ~550 °C transition step served to help eliminate possible carbon contaminations as the extraneous carbon structures would begin decomposing. However, the relatively stable a-AlO_x nanostructures would be unaffected at this temperature due to their kinetic entrapment architected by the high activation barrier for their phase transition, as reported in our earlier study.[21] Following this, the next transition step is chosen to investigate a partial conversion of the a-AlO_x nanostructures. Bearing in mind from our earlier works which demonstrated the conversion kinetics of the a-AlO_x nanostructures, we could observe that at a temperature of ~750 °C the particles could reliably undergo a phase conversion between 50 to 250 min of heating. Thus, the second transition step is initiated after heating to a temperature of ~750 °C for 2 h to ensure a ~50% conversion of the a-AlO_x nanostructures. Finally, the third transition step heated the sample to ~810 °C for 2 h to ensure a full conversion of the a-AlO_x nanostructures to the desired γ/θ-Al_2O_3. All heating experiments were performed at a ramp rate of ~50 °C min^{-1}, and samples were monitored isothermally so that no α-Al_2O_3 formed before cooling to room temperature. Transmission electron microscopy (TEM) was performed on a Zeiss Libra 200 MC operating at 200 kV, and elemental compositions and O/Al ratios were determined by statistical electron energy-loss spectroscopy (EELS) over ~25 particles per condition. TEM–EELS (Al $L_{2,3}$ and O K edges) was used throughout for quantitative O/Al evaluation and compositional statistics, providing an independent chemical confirmation of Al–O contributions relative to metallic Al signals in the nanocomposites. Additional spectroscopy that directly addresses oxidation state/bonding and coordination environments (XPS and ^{27}Al SSNMR) has been reported previously for this same class of LASiS-derived a-AlO_x/C NCs.[12,21]

3. Results and discussion

We present here an in-depth analysis of the LASiS-synthesized AlO_x metastable structures, and their thermally activated bond re-arrangements through a series of post-synthesis experiments involving Atomic Pair Distribution Function (PDF) analyses from X-ray scattering experiments. Specifically, analyze of the bond pair arrangements evolution at several time-steps throughout the material's high temperature transition from metastable to the first semi-stable polymorphic phases of γ/θ-Al_2O_3. By comparing the atomic bond arrangements as a function of their radial distributions for the initial material to those recorded at each stage of heating throughout the transition process, the relative change in instability and disorder-order transition could be tracked during the material's phase change. Fig. 1 shows an initial measurement using an Ag X-ray source to measure and calculate the material's PDF spectra. Using this as a starting point, we could proceed to measure and compare the initial average Al–O and Al–Al atomic radii to that of the sample at the beginning of their phase transition as well as their intermediate and final state of conversion to γ/θ-Al_2O_3. This allowed us to estimate the internal atomic coordination shifts as the material transitions from the meta-stable to semi-stable nanostructures.

Fig. 2 shows the systematic changes in the radial bond pair distributions ($G(r)$, $Å^{-2}$) for the samples exposed to different temperature regimes in an isochronous fashion as described in the methods section earlier. We observe that the synthesized

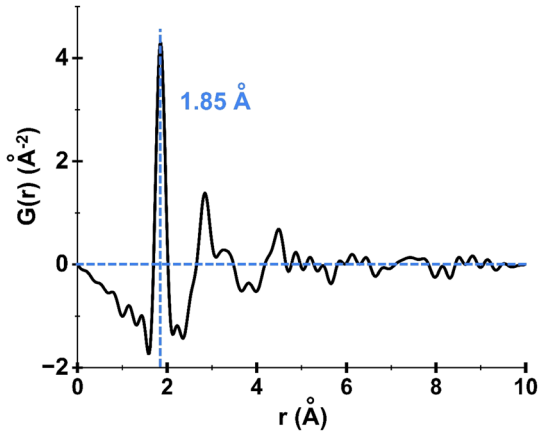

Fig. 1 PDF of a-AlO_x NCs showing an average Al–O distance of ~0.185 nm and a reasonable pairing of up to ~1 nm resolution.

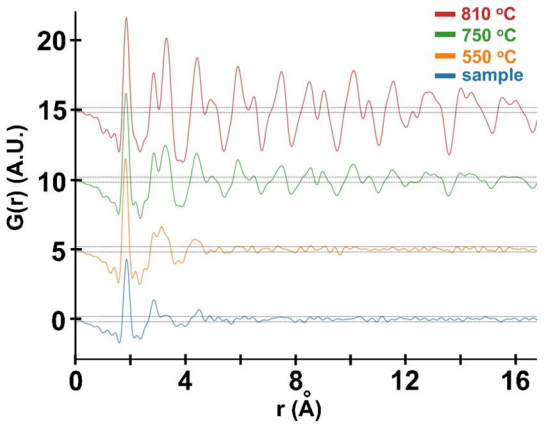

Fig. 2 X-ray pair distribution functions (PDFs), $G(r)$, of AlO_x/C nanocomposites showing temperature-driven structural evolution through transition steps 1–4 from room temperature to ~810 °C (RT, 550 °C, 750 °C, 810 °C). Traces are vertically offset for clarity; r is in Å. With increasing temperature, PDF features sharpen and extend to higher r, indicating increased structural ordering during the transition.

structures retain very little long-range order revealing the highly disordered and amorphous nature of the LASiS-synthesized material. For the first transition steps, we see that the long-range order does not increase which is to be expected as at low temperatures the metastable a-AlO_x structures should not change. As the temperature increases to 550 °C and 750 °C, the second and third transition steps start indicating slightly higher long-range orders in the $G(r)$ distributions. This culminates in the last transition step at 810 °C where distinct and repeatable long-range orders appear the most. It should be noted that the measurements in Fig. 2 indicate that in the last transition step of 810 °C, long-range orders could be differentiated to a radial distance of ~50Å, which is indicative of low order polycrystalline structures (see Fig. S1 in the SI).

Our initial data analyses involved refining and comparing the individual fits to the PDF data at the final temperature step 810 °C, with suspected alumina and aluminum hydroxide

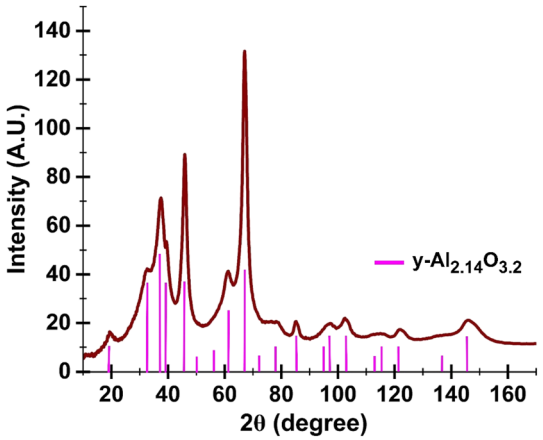

Fig. 3 X-ray diffraction (XRD) pattern (Cu K-α – equivalent) of the AlO_x/C nanocomposites after the final transition step (~810 °C), compared with reference γ-Al_2O_3 peak positions (tick marks) to confirm the crystalline endpoint used in the PDF analysis.

structures. However, rather than undertaking a trial and error approach, we converted the silver X-ray source data to equivalent copper k-alpha source data in order to compare to standard XRD peaks available for γ/θ-Al_2O_3 phase. This γ/θ-Al_2O_3 assignment is based on combined diffraction and total-scattering evidence where the converted XRD pattern is matched to the standard transition-alumina peak positions as reference, and the corresponding PDF evolution shows the emergence of alumina-like local/medium-range correlations at higher temperatures. Bearing this in mind, we report here the XRD and corresponding PDF data to establish the structural phase evolution, while oxidation state/bonding information is addressed *via* EELS and complementary spectroscopy measurements have been reported in our previous work[12] for the identical LASiS-synthesized a-AlO_x/C NC systems. As seen in Fig. 3, the XRD patterns and peak locations correlate fairly well with the standard peaks for a known semi-stable form of γ-$Al_{2.14}O_{3.2}$ at the final temperature step of 810 °C, where we expect a full conversion to γ/θ-Al_2O_3 phases.[28] This serves as a good validation for identifying the standard diffraction peaks for γ-Al_2O_3, thereby confirming that the transition in question did not overshoot and begin converting to the stable α-Al_2O_3.

Because the final transition step is the most structurally ordered state, the crystalline endpoint model used for PDF fitting is anchored to the XRD-identified transition-alumina phase. This XRD-matched model provides an internally consistent structural basis for interpreting the PDF peak assignments at the endpoint, while the earlier transition steps are discussed primarily in terms of relative changes in local Al–O correlations rather than unique atomistic structures. Complementary chemical-state/coordination evidence (XPS and ^{27}Al SSNMR) for this material class has been reported previously and is referenced here to avoid redundancy. With the XRD peaks for the polycrystalline structures of γ-$Al_{2.14}O_{3.2}$ being verified at the final transition step, we could then proceed to work backwards and create the theoretical PDF fit for γ-$Al_{2.14}O_{3.2}$ (green line in Fig. 4a) and match it with our

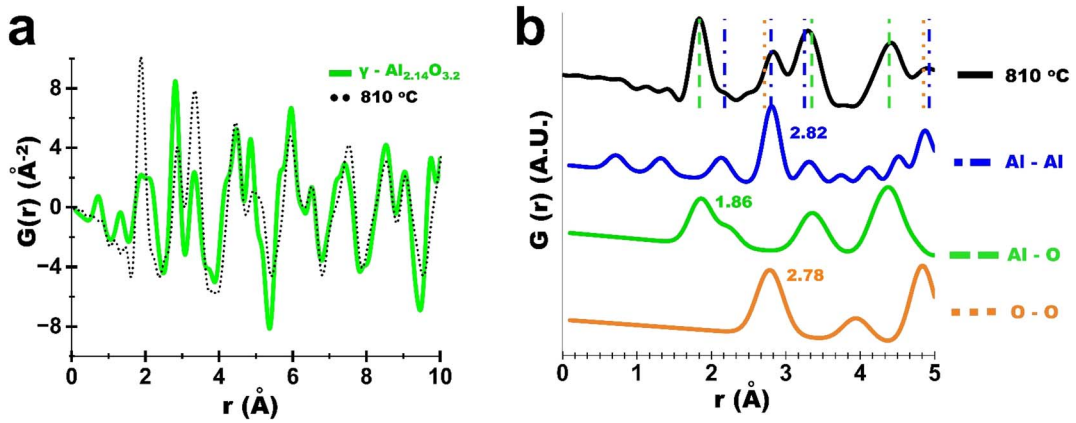

Fig. 4 PDF analysis using the XRD-matched structural model for the crystalline endpoint. (a) Experimental $G(r)$ for the final transition step (~810 °C) compared with the calculated PDF fit using the γ-$Al_{2.14}O_{3.2}$ model (difference/residual shown where applicable). (b) Decomposition of the calculated PDF from (a) into its elemental pair contributions (*e.g.*, Al–O, Al–Al, O–O), highlighting the nearest-neighbor features used for peak assignment and fitting.

experimentally observed PDF data. This match would then be used to identify the attributing elemental bond lengths associated with each peak position for the fully converted γ-Al_2O_3 samples. The PDF structures for the final transition of a-AlO_x at 810 °C, as seen in Fig. 4a (black line) indicated that the final measured experimental PDF peaks differ only slightly from those theoretical fit for standard γ-$Al_{2.14}O_{3.2}$ structures, although the XRD data seemed to match quite well. This could be attributed to a few reasons with the most plausible being a relatively high percentage of amorphous content that could reflect another structure. This would also explain why the fit begins to follow the matched γ-$Al_{2.14}O_{3.2}$ at longer order radii. By splitting the γ-$Al_{2.14}O_{3.2}$ PDF fit data into its relative elemental bond couples, as seen in Fig. 4b, we could decipher the elemental bond couples that deviate from the standard fit due to the various amorphous and disordered contents. In the PDF data plotted for the 810 °C transition step, it is clear that the Al–O bonds at the radial distance of ~1.86 Å show a significant increase in peak area when compared to corresponding bond pair (Al–O in green) that was matched with the γ-$Al_{2.14}O_{3.2}$ structures. This is concurrently met with a corresponding area decrease in the Al–Al radii peak at ~2.82 Å. At this stage, it is unclear whether this is due to the presence of another amorphous alumina/hydroxide structure or if it is due to the presence of remaining unreacted AlO_x structures. It is also possible that the matched γ-$Al_{2.14}O_{3.2}$ structure exhibits more bimodal behavior in the low order radii whereas experimentally the peaks are closer, thereby merging into one large peak instead of two smaller peaks.

Fig. 5a shows the final PDF for all four transition steps when compared with the matched known elemental bond couples overlaid in the lower order radial distance ranges (<5 Å). We see that as the transition step temperatures increase, the PDF peak intensities for Al–O and O–O bond pairs begin to sharpen. Furthermore, we see the emergence of a few of the longer order Al–O peaks particularly at the radii of ~3.25 Å and ~4.4 Å while the Al–Al bond radii stayed relatively constant. This indicates that the Al–Al bonds do not alter much as the material phase transition, but the Al–O bonds undergo distinct changes including coordination shifts and bond rearrangements. If we compare the Al–O first nearest neighbor radii in Fig. 5b, we see that the as-synthesized AlO_x sample starts very broad with a peak maxima at ~1.855 Å. Interestingly, at the first transition step of 550 °C, we observe a peak shift of ~0.043 Å to ~1.812 Å for the nearest neighbor Al–O bond pair. However, at this temperature it can be assumed that possibly there are no significant amorphous-to-crystalline structural changes within the AlO_x NPs as also indicated by the XRD data, but rather only the carbon structures burn off. This is likely due to some Al–Al bonds at ~2.1 Å from parasitic pure Al NPs, as also discussed in our earlier works,[12,21] that shift the peak slightly toward higher radii which oxidize at 550 °C. Once that excess carbon and Al NPs were accounted for, the remaining two transition steps could be used to observe the shift in coordination. At the third transition step or 750 °C, it is noticed that the partial transition of a-AlO_x to γ-Al_2O_3 results in a shift of ~0.02 Å, from ~1.812 Å to ~1.83 Å for the nearest neighbor Al–O bond pair peak. Finally, at the fourth transition step of 810 °C the full transition results in a further shift of ~0.01 Å from ~1.83 Å to ~1.84 Å. This can be explained by the emergence of the metastable AlO_x structures which comprise largely of a unique mix of AlO_4, AlO_5 and AlO_6 coordination, as observed in our earlier solid-state NMR results (discussed in detail in our earlier work),[12] gradually transition into the primarily AlO_6 coordinated γ-Al_2O_3 structures. In principle, deconvolving the first-shell Al–O PDF peak into explicit AlO_4, AlO_5, and AlO_6 contributions is possible. However, the centers and widths of these overlapping components can vary slightly with heat treatment due to bond-length distributions, evolving disorder, and the onset of medium-range ordering, making such a three-component fit highly covariant and potentially non-unique without additional independent constraints. Therefore, we adopted a conservative, data-driven approach by fitting and comparing the nearest-neighbor Al–O and first-neighbor Al–Al peaks using

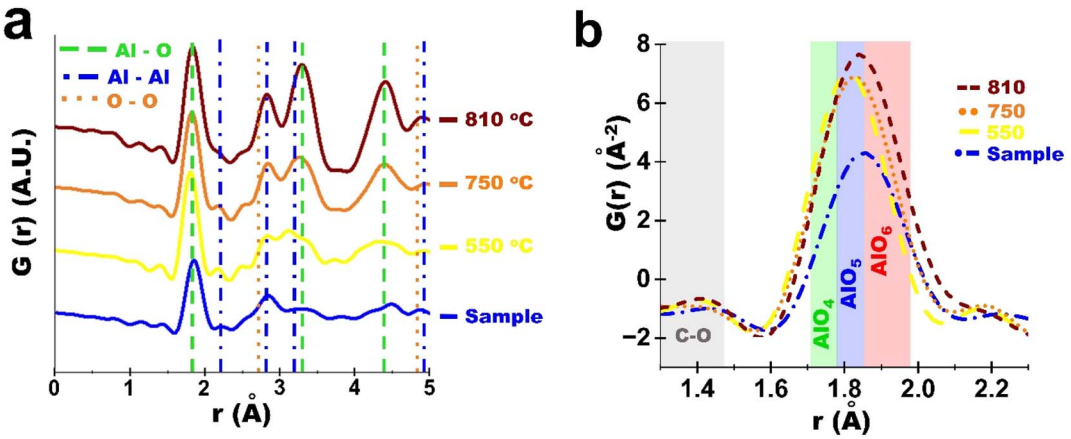

Fig. 5 Comparison of PDF data at transition steps. (a) Comparison of transition steps showing evolution of peak growth with respect to transition temperature showing a notable increase in sharpness and intensity for the Al–O and Al–Al first nearest neighbor peaks. (b) Comparison of transition steps showing evolution of Al–O bond pair peak with respect to transition temperature.

a consistent protocol; because both peaks are extracted from the same measurement and PDF reduction pipeline for each condition, their relative fitted intensities/areas provide a robust metric for changes in Al–O connectivity relative to the Al sub-network.[29–31] Using the ratio of the first nearest neighbor Al–O peak area to the bound Al–Al nearest neighbor peak area, we can calculate an average coordination number corresponding to the number of AlO_4, AlO_5 and AlO_6 coordination present in the structure (see Fig. S2 in SI). When calculated, the nearest neighbor PDF results in Fig. 5b for the final (810 °C) and third (750 °C) transition steps indicate an average coordination number of ~5 and ~4.78 respectively. Interestingly, this matches quite well to the expected 40–60% AlO_6 and 60–40% AlO_4/AlO_5 coordination ratio mix for the γ-Al_2O_3 polymorphic phase. In the case of the first two transition steps, however, the ratios are significantly higher with the ratio of the first and second transition steps being ~7.6 and ~8.2 respectively. Based on our earlier reported XPS results,[12] the ratio of the Al–O and Al–Al bond pair peak areas will justifiably be dependent on the relative amounts of each element in the composition (O/Al ~2.5–3.0 from earlier XPS analyses).[12] Thus, one can anticipate that AlO_x composition in the first two transition steps, with negligible phase transitions to γ-Al_2O_3, will plausibly have roughly twice the oxygen content as compared to the samples in the final transition stages (at 750 and 810 °C) which results in a significantly higher Al–O peak area, thereby distorting the average coordination ratio values. At this stage, we also believe that the increase in the coordination ratio between the first and second transition step can likely be attributed to the C–O at ~1.4 Å creating an indiscernible cumulative increase in the Al–Al bond peak.[32,33]

In a further effort to establish the sensitivity of laser parameters in LASiS experiments for tailoring the composition of these metastable a-AlO_x nanostructures, we present here a quantitative elemental analysis for the O/Al ratio at differing laser flux (J cm^{-2} ns^{-1} pulse width) conditions under which the initial a-AlO_x/C NCs were synthesized. To this end, we carried out statistical EELS measurements wherein the x ~ O/Al was estimated for ~25 different particles identified from TEM images and the results are for different laser fluences (J cm^{-2}) and pulse durations (ns). Fig. 6 shows TEM EELS spectra for the a-AlO_x/C NC samples synthesized *via* LASiS using the 5 ns laser comparing both ~0.15 and 0.2 J cm^{-2} ns^{-1} laser fluxes for the target ablation. Upon normalizing both spectra, we observe that the Al L_{23} peaks show similar relative intensities whereas the O_k peaks did not. The O_k peak for the ~0.15 J cm^{-2} ns^{-1} case showed substantially higher relative intensity. When comparing the calculated average scattering probabilities, as detailed in our previous work,[21] the ablation under ~0.15 J cm^{-2} ns^{-1} flux indicate a rough O/Al ratio of ~2.5 as compared to the samples from ~0.2 J cm^{-2} ns^{-1} flux ablation resulting in O/Al ~1.5. The Al L_{23} peak for the ~0.2 J cm^{-2} ns^{-1} case consequently also resembled the peak features of standard Al_2O_3, with a peak at ~76.5 eV (marked in Fig. 6 inset for Al L_{23} peak).

Our next investigation focused on the ability to tailor the specific O/Al ratio for the different a-AlO_x/C NCs synthesized *via* LASiS under varying laser flux conditions for all other parameters being kept identical. Initially, using two separate pulse duration lasers, we set the energy density to match each other with the hypothesis that this was the driving force for the reactions needed to make the O to Al ratio. However, what we found was that the resulting material was vastly different with O to Al ratios being higher in the 5 nano second case than the 9 nano second. We then went about matching the respective flux for each case instead, with the hypothesis being that it was the total amount of power dumped over time that is responsible for the production of the differing O to Al ratios. As seen in Fig. 7a, the use of two different lasers with pulse widths of ~5 and 9 ns respectively for the ablation during LASiS (described in detail in the methods section) result in a similar trend that matches the variations in O/Al ratios in the ensuing AlO_x samples as a function of laser flux. It should be noted that although the flux window appears moderate in absolute terms, it spans the full accessible operating range of our setup (~30–400 mJ per pulse), and the nanocomposite composition shows strong sensitivity within this window (most notably between 0.10 and 0.15 J cm^{-2}

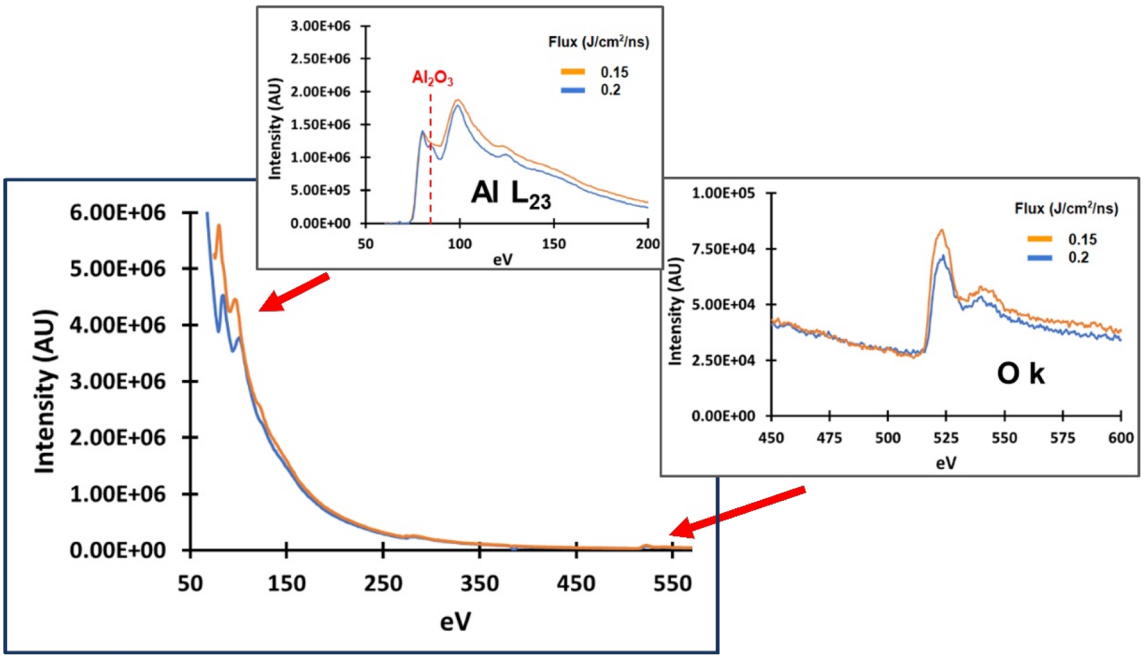

Fig. 6 TEM EELS spectra for two separate energy densities showing a decrease in measured O/Al ratio when laser flux is increased.

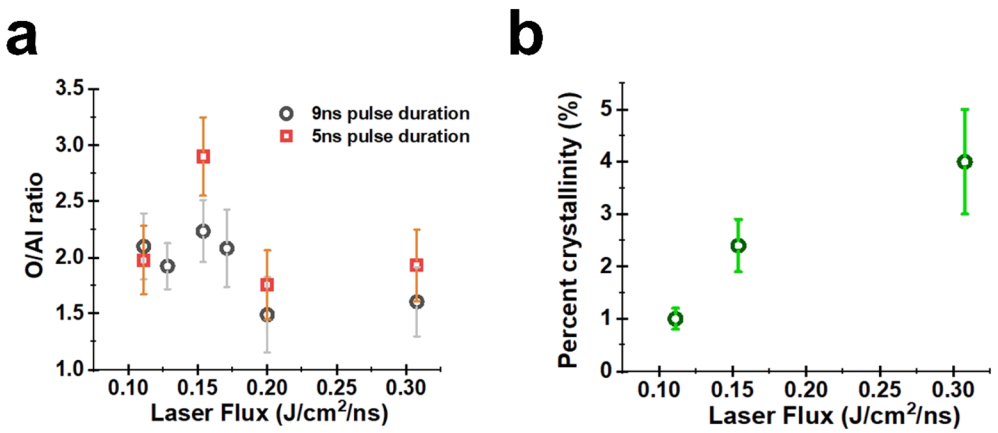

Fig. 7 Altering O/Al ratio and Al crystallinity using laser flux: (a) measured laser flux for two separate laser pulse durations *vs.* the resulting O/Al ratios. (b) Resulting Al crystallite percentage with differing laser flux.

ns^{-1}). The 5 ns and 9 ns datasets are treated as two discrete nanosecond pulse-duration conditions. Because flux is defined as fluence divided by pulse duration, matching flux at different τ requires different fluence (and thus different pulse energies for a fixed spot size), enabling a direct test of whether energy-delivery rate (flux) rather than pulse energy alone governs the resulting Al/O ratio. Notably, the composition response is most consistent when expressed *versus* flux, with both pulse durations yielding similarly high O/Al near ~0.15 J cm^{-2} ns^{-1} despite requiring different pulse energies to reach that condition. Fig. 7b shows the result of minor changes in the percentage of crystalline structures emerging in the AlO_x NCs under varying laser fluxes. As discussed in our earlier works, a small amount (<4% wt.) of parasitic crystalline Al forms during ablation which we have attributed to the median peak energy profile at the center of the Gaussian laser beam having enough power to fragment few chunks of pure Al particles. These minor chunks do not take part in the plasma driven reactions that result in the AlO_x production and are rather just tossed into solution after cavitation bubble collapse. The percentage of parasitic crystalline Al seems to increase as the flux increases due to the availability of a relatively greater amount of the peak beam power being above the laser fragmentation as the flux increases. In future experiments, we posit that the use of a hat-top beam shaper can possibly alleviate this parasitic crystalline Al formation due to uniform average power distribution across the beam profile. This should also result in a smaller deviation of the resulting O/Al ratios allowing for

greater tunability. The extent of crystalline/amorphous structures for the final NPs can also be controlled by tuning the organic solvent parameters (solvent choice, temperatures *etc.*) since these structural arrangements ensue once the particles exit the plume/cavitation bubble. Once the particles exit the cavitation bubble, they experience collisional growth until they reach a critical size, and the liquid cooling or quenching takes place. The cooling times for the ensuing particles in the liquid will affect their crystallinity, with longer cooling times required for the nucleation and formation of stable crystallites. By tuning this cooling rate, it may be possible to not only control the crystalline or amorphous nature of the ensuing NPs, but also the specific type of crystallite phases that are formed. Such tuning of the cooling rates are possible by controlling both the solvent densities and temperatures through suitable choices of solvents (acetone, toluene, methanol, *etc.*).[13]

Tunability, repeatability and uniformity of samples have long been key issues with LASiS-based synthesis.[34,35] Bearing in mind that the formation of the initial AlO_x clusters greatly depends on the input laser flux, uniformity of peak power across beam profiles and hence, the resulting plasma temperatures,[23,24] we resort to a mechanism to filter out the low and high regions of the laser flux distribution across the beam profile. Typically, the laser used for ablation during LASiS is thought of as only a means of dumping energy onto the liquid-confined target to induce a high temperature plasma; however, herein our interest is to investigate the role of laser beam profile in architecting the structure–composition homogeneity in the NPs formed. The beam energy profile used for synthesis of the *m*-AlO_x NPs was a Gaussian energy profile. It can be assumed that the laser energy density varies drastically throughout the output beam profile. The energy at the outer edges of the Gaussian shaped beam can be presumably far too low to induce laser-target coupling for ablation to ensue, while the energy density at the center of the beam can rise to a significantly high value for initiating metal fragmentation. At the relatively low flux (<~2–3 J cm^{-2} ns^{-1}) where AlO_x NPs are formed, the plasma geometry behaves more like a disk than a perfect sphere with high and low energy regions at the center and edge resulting from the Gaussian energy profile. For this reason, we hypothesize that the correct energy density/flux needed for the synthesis of primarily AlO_x NPs is likely where the average flux across the greatest area of the Gaussian energy profile resides. This implies that the center and the edges of the Gaussian beam cross-section can end up producing large amount of parasitic and undesirable structures resulting in the low homogeneity and uniformity of the samples.

It should be highlighted that another key difference observed in Fig. 7a is the variations in the average uncertainties in the data for the O/Al ratios obtained from ablation using the 9 ns and the 5 ns pulse width lasers. The average O/Al ratios along with the standard deviations in the average values, measured for the ~25 different particles using HRTEM EELS on each sample made at different laser fluxes, used earlier could be used as a statistical metrics to describe the homogeneity if the as-synthesized AlO_x samples. What we noticed was that across nearly all the sample cases, the 9 ns laser demonstrated a slightly lower variances in

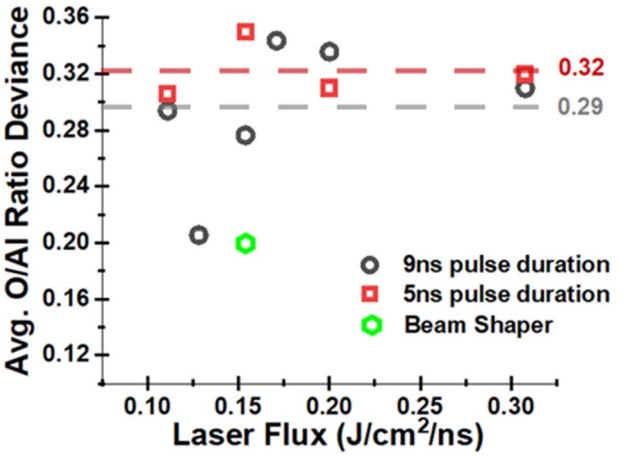

Fig. 8 O/Al ratio deviance for 9 ns laser demonstrated a lower standard deviation across sampled NPs than the 5 ns laser. Flat top beam shaped decreased the standard deviation at 0.15 J cm^{-2} ns^{-1}.

the average O/Al ratios when compared to the results from the 5 ns laser, with the average standard variance ranging between ~0.29 and 0.32 in the case of the 5 ns laser (see Fig. 8). Upon closer inspection it was found that the cross-sectional beam power distribution for the 5 ns laser was significantly more Gaussian than the 9 ns laser. In contrast, the 9 ns laser beam had less median peak power and a more evenly distributed profile. To validate our earlier hypothesis on the effect of power distribution across laser beam profiles on the compositional variations in the ensuing AlO_x NPs, we also carried out some preliminary experiments by introducing a flat top beam shaper into the laser beam line as described in the methods section. The use of the beam shaper should result in an even spread of plasma temperature and reduce the overall amount of undesirable contaminant structures while increasing homogeneity throughout the samples as discussed. We present here a test case run for the synthesis of the a-AlO_x/C NCs under ablation at ~0.15 J cm^{-2} ns^{-1} laser flux using a hat-top beam shaper coupled with the Gaussian 5 ns laser beam which clearly resulted in a ~43% decrease in average standards deviances (from 0.35 to 0.2) for the O/Al ratios. However, this came with a compromise that although the average deviances in the data decreased, the average O/Al ratio also decreased from ~2.9 to ~1.7. In sum, the addition of the beam shaper did achieve an increase in the sample homogeneity to support our hypothesis, however it left us with a new challenge from these observations that would indicate this also alters the power distribution profile and will likely have to be compensated with an increase in the average laser flux to achieve the optimum O/Al ratios of ~3.0. At this stage, we reserve more systematic studies in future to provide conclusive and robust insights into the role of laser flux and beam structuring in compensating these non-linear optical phenomena during LASiS.

4. Conclusion

In conclusion, we have implemented HTXRD and HRTEM in analyzing the phase change of a metastable AlO_x NC to the

slightly more globally stable alumina polymorph γ/θ-Al_2O_3. The premise for the phase change and the materials studied in this publication were briefly discussed in our previous publication. Atomic Pair Distribution Function (PDF) analysis from X-ray scattering experiments were implemented to further understand the structural changes in metastable AlO_x NCs. Several transition steps were used to track the phase change including heating the NCs to ~550 °C to eliminate carbon contamination, ~750 °C for partial conversion, and ~810 °C for full conversion to γ-Al_2O_3. The material's structure evolved from highly disordered to low-order polycrystalline as temperature increased. Changes in Al–O bonds indicated coordination shifts during each transition step which provided insights into the stability and structural changes of AlO_x nanocomposites during heating. We also demonstrated the ability to achieve varying O/Al ratios (~1.5–3.0) and percentage crystallinity by altering the laser fluxes (~0.1–0.3 J cm^{-2} ns^{-1}) as a preliminary effort toward controlling the material's phase-change behavior and amount of off-gassing during its phase transition. Additionally, we were able to increase the relative homogeneity of the synthesized material by implementing a flat top beam shaped during ablation. The flat top bean shaped was shown to make more uniform ablation and plasma conditions across the area of the beam resulting in smaller deviation in measured O/Al ratios but also resulted in a decrease in overall O/Al ratio. Overall, this work strengthens our understanding of the laser flux sensitivity during the LASiS process within the nanosecond pulse regimes and highlights how even moderately controlled changes in laser parameters can influence the structure–composition properties of the a-AlO_x/C nanocomposites. In turn this provides our current motivations for further future investigations into other laser pulse regimes and their effects on the non-equilibrium LASiS techniques.

Conflicts of interest

There are no conflicts to declare.

Data availability

The data used throughout the publication was collected in whole by the authors and will be provided upon fair request to the corresponding author.

Supplementary information (SI) is available. See DOI: https://doi.org/10.1039/d5ra07897k.

Acknowledgements

The works carried out by E. D. and D. M. were supported by grants from Air Force Office of Scientific Research (AFOSR) through award no.: FA9550-19-1-0366 (E. D. and D. M.). We acknowledge the core XRD and Microscopy facilities and the Institute for Advanced Materials and Manufacturing (IAMM) at the University of Tennessee, Knoxville, for access to and assistance with various instruments. We would also like to acknowledge the technical and research assistance from Dr Michael Koehler, Dr Claudia Rawn, Dr Peter Metz and Dr Gerd Duscher at the Institute for Advanced Materials and Manufacturing (IAMM).

References

1 A. Allemand, C. Guerin, C. Besnard, R. Billard and Y. Le Petitcorps, A comparison between a new Ultra Fast Pressureless Sintering (UFPS) technology and Spark Plasma Sintering (SPS) for Barium AluminoSilicate metastable phase, *J. Eur. Ceram. Soc.*, 2021, **41**, 1524–1529, DOI: 10.1016/j.jeurceramsoc.2020.09.054.

2 J. Badding, L. Parker and D. Nesting, High pressure synthesis of metastable materials, *J. Solid State Chem.*, 1995, **117**, 229–235.

3 P. Maneeratanasarn, K. Tran Van, S. Y. Kim, B. G. Choi and K. B. Shim, Synthesis of phase-controlled iron oxide nanoparticles by pulsed laser ablation in different liquid media, *Phys. Status Solidi A*, 2013, **210**, 563–569, DOI: 10.1002/pssa.201228427.

4 V. Amendola, *et al.*, Room-Temperature Laser Synthesis in Liquid of Oxide, Metal-Oxide Core-Shells, and Doped Oxide Nanoparticles, *Chem. - Eur. J.*, 2020, **26**, 9206–9242, DOI: 10.1002/chem.202000686.

5 D. S. Zhang, B. Goekce and S. Barcikowski, Laser Synthesis and Processing of Colloids: Fundamentals and Applications, *Chem. Rev.*, 2017, **117**, 3990–4103, DOI: 10.1021/acs.chemrev.6b00468.

6 S. Reich, *et al.*, Fluence Threshold Behaviour on Ablation and Bubble Formation in Pulsed Laser Ablation in Liquids, *Chemphyschem*, 2017, **18**, 1084–1090, DOI: 10.1002/cphc.201601198.

7 N. Lasemi, U. Pacher, C. Rentenberger, O. Bomatí-Miguel and W. Kautek, Laser-Assisted Synthesis of Colloidal Ni/NiOx Core/Shell Nanoparticles in Water and Alcoholic Solvents, *ChemPhysChem*, 2017, **18**, 1118–1124, DOI: 10.1002/cphc.201601181.

8 V. Amendola and S. Barcikowski, A quarter-century of nanoparticle generation by lasers in liquids: Where are we now, and what's next?, *J. Colloid Interface Sci.*, 2017, **489**, 1–2, DOI: 10.1016/j.jcis.2016.12.016.

9 A. Matsumoto, *et al.*, Transfer of the Species Dissolved in a Liquid into Laser Ablation Plasma: An Approach Using Emission Spectroscopy, *J. Phys. Chem. C*, 2015, **119**, 26506–26511, DOI: 10.1021/acs.jpcc.5b07769.

10 S. Barcikowski and F. Mafuné, Trends and Current Topics in the Field of Laser Ablation and Nanoparticle Generation in Liquids, *J. Phys. Chem. C*, 2011, **115**, 4985, DOI: 10.1021/jp111036a.

11 E. M. Davis, *et al.*, Fe-carbide/Fe-oxide-based nanocomposites synthesized as magnetic nanomaterials via laser ablation synthesis in solution (LASiS), *Appl. Surf. Sci.*, 2024, **658**, 159682, DOI: 10.1016/j.apsusc.2024.159682.

12 E. M. Davis, G. Duscher, J. Wen and D. Mukherjee, Laser-Induced Trapping of Metastable Amorphous AlOx/C ($2.5 < x \leq 3.5$) Nanocomposites: Implications for Use as Solid Phase Gas Generators, *ACS Appl. Nano Mater.*, 2023, **6**, 10977–10985, DOI: 10.1021/acsanm.3c00473.

13 S. A. Davari, *et al.*, Graphitic coated Al nanoparticles manufactured as superior energetic materials via laser ablation synthesis in organic solvents, *Appl. Surf. Sci.*, 2019, **473**, 156–163, DOI: 10.1016/j.apsusc.2018.11.238.
14 S. Hu, *et al.*, Hybrid nanocomposites of nanostructured Co3O4 interfaced with reduced/nitrogen-doped graphene oxides for selective improvements in electrocatalytic and/or supercapacitive properties, *RSC Adv.*, 2017, **7**, 33166–33176, DOI: 10.1039/c7ra05494g.
15 S. Hu, C. Melton and D. Mukherjee, A facile route for the synthesis of nanostructured oxides and hydroxides of cobalt using laser ablation synthesis in solution (LASIS), *Phys. Chem. Chem. Phys.*, 2014, **16**, 24034–24044.
16 S. Hu, *et al.*, A facile and surfactant-free route for nanomanufacturing of tailored ternary nanoalloys as superior oxygen reduction reaction electrocatalysts, *Catal. Sci. Technol.*, 2017, **7**, 2074–2086, DOI: 10.1039/c7cy00073a.
17 S. Hu, M. Tian, E. L. Ribeiro, G. Duscher and D. Mukherjee, Tandem laser ablation synthesis in solution-galvanic replacement reaction (LASiS-GRR) for the production of PtCo nanoalloys as oxygen reduction electrocatalysts, *J. Power Sources*, 2016, **306**, 413–423, DOI: 10.1016/j.jpowsour.2015.11.078.
18 S. Hu, G. Goenaga, C. Melton, T. A. Zawodzinski and D. Mukherjee, PtCo/CoOx nanocomposites: Bifunctional electrocatalysts for oxygen reduction and evolution reactions synthesized via tandem laser ablation synthesis in solution-galvanic replacement reactions, *Appl. Catal., B*, 2016, **182**, 286–296, DOI: 10.1016/j.apcatb.2015.09.035.
19 E. L. Ribeiro, *et al.*, MOF-derived PtCo/Co3O4 nanocomposites in carbonaceous matrices as high-performance ORR electrocatalysts synthesized via laser ablation techniques, *Catal. Sci. Technol.*, 2021, **11**, 3002–3013, DOI: 10.1039/D0CY02099K.
20 E. L. Ribeiro, S. A. Davari, S. Hu, D. Mukherjee and B. Khomami, Laser-induced synthesis of ZIF-67: a facile approach for the fabrication of crystalline MOFs with tailored size and geometry, *Mater. Chem. Front.*, 2019, **3**, 1302–1309, DOI: 10.1039/C8QM00671G.
21 E. M. Davis, C. Rawn, M. G. Boebinger and D. Mukherjee, Kinetic analyses for solid-state phase transition of metastable amorphous-AlOx ($2.5 < x \leq 3.0$) nanostructures into crystalline alumina polymorphs, *Sci. Rep.*, 2025, **15**, 7854, DOI: 10.1038/s41598-025-90586-z.
22 A. Fallahi, G. Guldentops, M. Tao, S. Granados-Focil and S. Van Dessel, Review on solid-solid phase change materials for thermal energy storage: Molecular structure and thermal properties, *Appl. Therm. Eng.*, 2017, **127**, 1427–1441.
23 P. Hai and C. Wu, A comparative DFT study of the oxidation of Al crystals and nanoparticles, *Phys. Chem. Chem. Phys.*, 2021, **23**, 24004–24015, DOI: 10.1039/D1CP03241K.
24 J. Lam, D. Amans, C. Dujardin, G. Ledoux and A.-R. Allouche, Atomistic Mechanisms for the Nucleation of Aluminum Oxide Nanoparticles, *J. Phys. Chem. A*, 2015, **119**, 8944–8949, DOI: 10.1021/acs.jpca.5b05829.
25 V. Amendola and M. Meneghetti, What controls the composition and the structure of nanomaterials generated by laser ablation in liquid solution?, *Phys. Chem. Chem. Phys.*, 2013, **15**, 3027–3046, DOI: 10.1039/c2cp42895d.
26 L. M. Frias Batista, *et al.*, How Pulse Width Affects Laser Ablation of Organic Liquids, *J. Phys. Chem. B*, 2023, **127**, 6551–6561, DOI: 10.1021/acs.jpcb.3c03708.
27 P. C. Metz, M. R. Koehler and K. Page, Data quality in laboratory convergent-beam X-ray total scattering, *J. Appl. Crystallogr.*, 2024, **57**, 1566–1577.
28 R.-S. Zhou and R. L. Snyder, Structures and transformation mechanisms of the η, γ and θ transition aluminas, *Acta Crystallogr., Sect. B:Struct. Sci.*, 1991, **47**, 617–630.
29 V. Petkov, Pair distribution functions analysis, *Characterization of Materials 1361*, 2012.
30 S. Kajita, S. Kohara, Y. Onodera, T. Fukunaga and E. Matsubara, Structural analysis of Pd-Cu-Si metallic glassy alloy thin films with varying glass transition temperature, *Mater. Trans.*, 2011, **52**, 1349–1355.
31 I. Romero-Muñiz, E. Loukopoulos, Y. Xiong, F. Zamora and A. E. Platero-Prats, Exploring porous structures without crystals: advancements with pair distribution function in metal-and covalent organic frameworks, *Chem. Soc. Rev.*, 2024, **53**(24), 11772–11803.
32 M. W. Terban and S. J. L. Billinge, Structural Analysis of Molecular Materials Using the Pair Distribution Function, *Chem. Rev.*, 2022, **122**, 1208–1272, DOI: 10.1021/acs.chemrev.1c00237.
33 V. Petkov, Y. Ren, S. Kabekkodu and D. Murphy, Atomic pair distribution functions analysis of disordered low-Z materials, *Phys. Chem. Chem. Phys.*, 2013, **15**, 8544–8554.
34 S.-X. Liang, L.-C. Zhang, S. Reichenberger and S. Barcikowski, Design and perspective of amorphous metal nanoparticles from laser synthesis and processing, *Phys. Chem. Chem. Phys.*, 2021, **23**, 11121–11154, DOI: 10.1039/D1CP00701G.
35 S. Barcikowski and G. Compagnini, Advanced nanoparticle generation and excitation by lasers in liquids, *Phys. Chem. Chem. Phys.*, 2013, **15**, 3022–3026, DOI: 10.1039/c2cp90132c.